Flexible membrane boundary condition DEM-FEM for drained and undrained monotonic and cyclic triaxial tests

Tarek Mohamed, Jérôme Duriez, Guillaume Veylon, Laurent Peyras

Flexible membrane boundary condition DEM-FEM for drained and undrained monotonic and cyclic triaxial tests

Tarek Mohamed[1,2*], Jérôme Duriez[2], Guillaume veylon[2], Laurent Peyras[2]

[1*]Laboratoire de Mécanique, Modélisation et Procédés Propres (M2P2), Aix Marseille Univ, 38 Rue Frédéric Joliot Curie, Marseille, 13013 , France.

[2*]INRAE, Aix Marseille Univ, RECOVER, Aix-en-Provence, France.

*Corresponding author(s). E-mail(s): tarek.MOHAMED@univ-amu.fr;

Abstract

Accurate simulation of laboratory undrained and cyclic triaxial tests on granular materials using the Discrete Element Method (DEM) is a crucial concern. The evolution of shear bands and non-uniform stress distribution, affected by the membrane boundary condition, can significantly impact the mechanical behavior of samples. In this work, the flexible membrane is simulated by using the Finite Element Method (FEM) coupled with DEM. In addition, we introduce a hydro-mechanical coupling scheme with a compressible fluid to reproduce the different undrained laboratory tests by using the membrane boundary. The evolution of pore pressure is computed incrementally based on the variation of volumetric strain inside the sample. The results of the membrane boundary condition are compared with more classical DEM simulations such as rigid wall and periodic boundaries. The comparison at different scales reveals many differences, such as the initial anisotropic value for a given preparation procedure, fabric evolution, volumetric strain and the formation of shear bands. Notably, the flexible boundary exhibits more benefits and better aligns with experimental data. As for the undrained condition, the results of the membrane condition are compared with experimental data of Toyoura sand and rigid wall boundary with constant volume.

Finally, stress heterogeneity during undrained monotonic and cyclic conditions using the membrane boundary is highlighted.

Keywords: Membrane boundary condition, DEM, Shear band, Anisotropy, Undrained cyclic triaxial test

1 Introduction

The Discrete Element Method (DEM) is frequently used to simulate triaxial tests. In conventional DEM simulations of triaxial tests, rigid wall enclosing parallelepiped specimens [e.g., 18, 19] or periodic boundaries [5, 23] are commonly applied. However, flexible boundary conditions are often employed in laboratory triaxial tests. This preference for the rigid or periodic boundaries in DEM simulations is primarily driven by the simplicity they offer in the simulation process. While a periodic boundary describes the infinite domain by characterizing it through the repetition of a cell pattern that periodically replicates in infinite space, Representative Volume Elements (RVEs). The main feature of the periodic boundary is to eliminate the boundary effects. Also as highlighted by [5], the periodic boundary gives different volumetric strain than the physical sample. Additionally, a common characteristic shared by rigid and periodic boundaries is their inability to accurately capture the evolution of shear bands observed in laboratory triaxial tests. On the other hand, the flexible membrane boundary can affect the mechanical behavior of triaxial samples [12], especially when dealing with materials that undergo large deformations. A flexible latex membrane allows the material to deform freely during testing and form shear bands [28]. The incorporation of a flexible membrane in DEM simulations of triaxial tests leads to a more accurate representation of the laboratory test, as it deals with specific boundary-dependent phenomena, i.e., BVP, rather than a pure soil response.

Attempts are made to reproduce flexible membrane by bonded particles in DEM, known as the bonded-ball membrane [3, 7, 11, 21, 32]. Although the bonded-ball membrane method has the capability to include membrane effects, such as the evolution of shear bands, current algorithms face challenges, particularly in establishing a reliable numerical representation for the deformation properties of an actual membrane. On the other hand, several researchers have undertaken the coupling of the DEM and Finite Element method (FEM) to investigate the interaction between particulate materials and various shell elements. For example, [29] specifically examined the reinforcement of earth structures with geosynthetic sheets by employing the coupled approach of the FEM and DEM. Also, [22] used a 2D polygonal DEM-FEM interface coupling to study the failure analysis of a concrete faced rockfill dam under earthquake effect. In this work we propose a FEM-based membrane implementation with a direct description of membrane action shell based on the actual elastic properties, thickness and density of the laboratory latex membrane.

Furthermore, the undrained condition is implemented to be applied within the membrane boundary, allowing the estimation of excess pore pressure based on volumetric changes. While, maintaining a constant volume condition, as applied in [16], is not suitable in this context for several reasons as discussed by [15]. Firstly, the undrained condition differs from a constant-volume state, even under complete soil saturation, allowing for minor volume changes without fluid inflow or outflow. Secondly, the constant-volume approximation is unsuitable for unsaturated conditions where the volumetric stiffness of pore fluid mixture might be smaller than the bulk stiffness of the soil skeleton, limiting its applicability. Thirdly, the constant volume assumption hampers the simulation of intricate loading and stress paths encountered in field or laboratory settings, Since maintaining a constant volume represents a strain-control condition that is not always present in laboratory tests, the control mode, whether stress, strain, or a combination of both as in the conventional drained triaxial compression test, may influence only instability or failure conditions [9, 25].

As such, the combined objective of this paper is to propose a comprehensive method for simulating triaxial tests under both drained and undrained conditions by using a membrane boundary. This article is structured into three sections. Section 2 presents the used DEM-FEM coupling method, the strain matrix of DEM samples with flexible membrane and the implementation of the undrained condition. Section 3 presents the numerical packing and different samples generation as well as a comparison between the different boundary conditions for drained triaxial tests at both macro and micro scales for loose and relatively dense samples of Toyoura sand including laboratory results. Finally, Section 4 presents simulations of undrained triaxial tests using flexible boundaries for both monotonic and cyclic loading. The results are then compared with undrained triaxial tests conducted on Toyoura sand.

2 DEM-FEM numerical model for membrane boundary with excess pore pressure evolution

2.1 Finite element method modelling of flexible membrane

The conventional triaxial test configuration involves a cylindrical soil sample vertically enclosed by a thin latex membrane clamped to the top and bottom platens. In this section, a robust flexible membrane model is used to correctly mimic the laboratory triaxial test inside 3D-DEM numerical simulations. A constant strain triangle (CST) finite element with three node points is used to build the membrane in Flac3D [14]. The CST element assumes a plane stress configuration typical of thin structures and considers two translational degrees of freedom for each node, introducing membrane action to the shell elements. The shell elements are considered as an isotropic elastic material characterized by Young's modulus E and Poisson's coefficient ν. The thickness t is required to characterize the rigidity of the shell element needed to form the finite element stiffness matrix of the shell. Unlike Flac3D zones which use the finite volume concept, membrane elements are modeled using Finite Element Analysis. The discretization and time integral of the governing equation uses the classical finite element method FEM for triangular element [4] with central-difference method for time integration. The dynamic response equations of a structure element can be obtained by ensuring that the external work is absorbed by the internal work as follows:

$$\begin{aligned}\int_{V_e} \left\{\delta\mathbf{u}\right\}^T \left\{\mathbf{F}\right\} dV + \int_{S_e} \left\{\delta\mathbf{u}\right\}^T \left\{\mathbf{\Phi}\right\} dS + \sum_{i=1}^{n} \left\{\delta\mathbf{u}\right\}_i^T \left\{\mathbf{p}\right\}_i = \\ \int_{V_e} \left(\left\{\delta\epsilon\right\}^T \left\{\sigma\right\} + \left\{\delta\mathbf{u}\right\}^T \rho \left\{\ddot{\mathbf{u}}\right\} + \left\{\delta\mathbf{u}\right\}^T \kappa_d \left\{\dot{\mathbf{u}}\right\} \right) dV\end{aligned} \tag{1}$$

where $\mathbf{F}$, $\mathbf{\Phi}$ and $\mathbf{p}$ denote body force per unit volume, applied pressure and nodal concentrated force, respectively and κ_d is a material-damping parameter. $\mathbf{u}$ is the displacement field. The left side of the Eq. 1 represents the external work. Eq. 1 can be recast in a different form after defining in particular a mass $\mathbf{M}$ and damping $\mathbf{c}$ matrix as follows:

$$[\mathbf{m}] = \int_{V_e} \rho [\mathbf{N}]^T [\mathbf{N}]\, dV \tag{2}$$

$$[\mathbf{c}] = \int_{V_e} \kappa_d [\mathbf{N}]^T [\mathbf{N}]\, dV \tag{3}$$

The internal force for a triangular element is defined as:

$$\left\{\mathbf{r}^{int}\right\} = \int_{V_e} \left[\mathbf{B}\right]^T \left\{\sigma_{\mathbf{m}}\right\} dV \tag{4}$$

$$\left\{\sigma_m\right\} = \frac{1}{t}\begin{Bmatrix} N_x \\ N_y \\ N_{xy} \end{Bmatrix}_m = \left[\boldsymbol{E}_m\right]\left\{\boldsymbol{\varepsilon}\right\} = \begin{bmatrix} \frac{E}{1-\nu^2} & \nu\left(\frac{E}{1-\nu^2}\right) & 0 \\ & \frac{E}{1-\nu^2} & 0 \\ sym. & & \frac{E}{2(1+\nu)} \end{bmatrix}\begin{Bmatrix} \varepsilon_x \\ \varepsilon_y \\ \gamma_{xy} \end{Bmatrix} \tag{5}$$

where braces denote vectors and square brackets denote matrices. $[\mathbf{N}]$ is the shape function matrix [4] and matrix $[\mathbf{B}]$ is the strain-displacement matrix that relates the the strain of the element and the displacements at each nodes $\{\delta\epsilon\} = [\mathbf{B}]\{\mathbf{d}\}$. The membrane resultants N_x, N_y and N_{xy} have units of forces per unit length. E_m is the membrane stiffness matrix. In this section x and y are the local axes forming the triangular element plane. The internal forces $\mathbf{r}^{int}$ for a single membrane element is :

$$\left\{\mathbf{r}^{int}\right\} = \left[\mathbf{B}\right]^T\left\{\boldsymbol{E}_m\right\}\left[\mathbf{B}\right]\left[\mathbf{d}\right] A.t \tag{6}$$

Where A is the area of the triangular element. Finally, the whole stiffness matrix of the structure is established as follows:

$$\left[\mathbf{M}\right]\left\{\ddot{\mathbf{D}}\right\} + \left[\mathbf{C}\right]\left\{\dot{\mathbf{D}}\right\} = \left\{\mathbf{R}^{ext}\right\} - \left\{\mathbf{R}^{int}\right\} \tag{7}$$

where $\left\{\mathbf{R}^{int}\right\}$ is the sum of $\left\{\mathbf{r}^{int}\right\}$ of each element. $\left\{\mathbf{R}^{ext}\right\}$ is the sum of all applied forces and pressure on nodes for the whole structure.

2.2 DEM Contact model and interaction between DEM and FEM triangular element

In this study, the rolling resistance contact model [13] is used with spherical particles to model Toyoura sand mechanical behavior as presented in [18]. The contact model comprises four parameters: normal and tangential stiffness, denoted as K_n and K_s

respectively, along with Coulomb and rolling friction coefficients μ and μ_r. The details of the contact model between particles and between particles-membrane are outlined in Appendix A.

The interaction between particles and the membrane occurs by detecting the contact between particles and shell elements. The execution of the interaction between DEM particles and the membrane FEM element involves converting contact forces and moments to equivalent nodal forces $\left\{\mathbf{p}\right\}_i$ for triangular FEM elements see Eq. 1. Note that at the contact level, the rolling resistance moment used here has no twisting component M_n as shown in Fig. 1. As illustrated in Fig. 1, each node presents three unknown forces in the $\boldsymbol{n}$ (triangle normal), shear direction $\boldsymbol{s} = \frac{\boldsymbol{F}^{shear}}{|F^{shear}|}$, and $\boldsymbol{t}$ directions, forming an indeterminate system of equations. This leads to a total of 9 unknowns for each triangular element. It's important to note that the nodal forces will balance both the contact forces and the rolling moment at the point of contact. Equilibrium static equation of the element can provide 6 equations to solve 9 unknowns. In addition, the barycentric weighting $ni = \frac{Ai}{A_1+A_2+A_3}$ as shown in Fig. 1 is applied to offer 2 additional equations to find the nodal reactions in s direction. The final required equation is that the sum of the products of the distances $d_{i,t}$ from contact point and the forces applied at the vertices in the $\mathbf{t}$ direction being equal to zero. $\sum p_{i,t} d_{i,t} = 0$.

On the other hand, the membrane element logic employs an explicit, direct integration method to discretize Eq. 7 in time at the same timestep as DEM calculation. The critical time step can also be computed separately for each membrane element and DEM particle, taking into account translation and rotational motions, and finally considering a minimum critical time step across DEM and FEM elements.

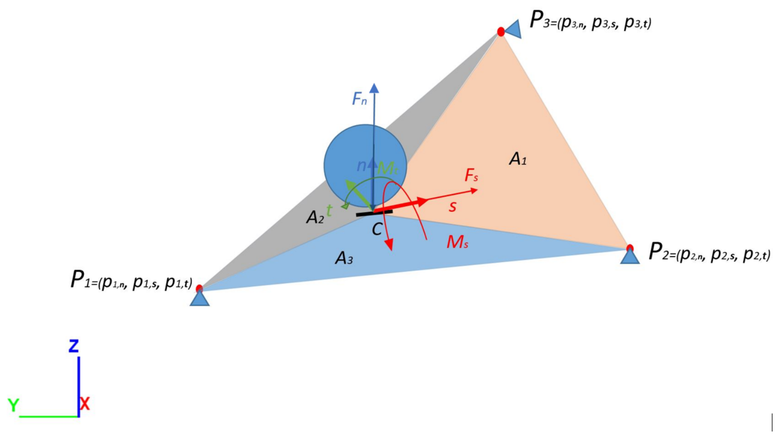

Fig. 1 Contact between a granular particle and a triangular element. The contact forces and moments are transmitted to the nodes of the triangular element.

2.3 Calculations of strain matrix and volumetric strain for a sample with a flexible boundary

Unlike parallelepiped specimens enclosed within rigid boundaries, assessing the volume of a deformed specimen delimited by a membrane is not straightforward and various methods have been proposed in the literature to quantify the variation in volumetric strain for cylindrical shapes with irregular outer shells. [16] used Gauss divergence theorem to calculate the volume of specimens bounded by a membrane from triangle elements. The sample volume, denoted as V_s, of a cylindrical sample with a membrane made of triangular elements can be calculated as follows:

$$Vs = \iiint_V dv = \frac{1}{3}\iint_s \boldsymbol{n}.\boldsymbol{x} ds = \frac{1}{3}\sum_{c\in S} \boldsymbol{n_c}.\boldsymbol{x_c} A_c \tag{8}$$

where S is the surface of the closed specimen space, including the top and bottom loading plates. For a triangle element on the membrane surface, the centroid position $\boldsymbol{x_c}$ is computed by averaging the positions of its constituent nodes. $\boldsymbol{n_c}$ and A_c denote the outward normal and area of the corresponding triangle. Additionally, [32] measured volumetric changes by dividing the sample center into three regions. Two cones were formed from the center towards the upper and bottom platens, while the third region constituted the remaining cylindrical sample enclosed by the deformed flexible membrane. The volume of this third region is calculated as the sum of all the volumes of the 3D Simplices formed by the triangles and the center of the sample.

In this study, our scope extends beyond solely assessing changes in volumetric strain. We additionally compute all components of the strain matrix from particle velocities to comprehensively examine strain elements across different tests, including the evaluation of ϵ_{xx} and ϵ_{yy} during undrained triaxial tests (see Section 4 below). Therefore, the strain rate tensor $\dot{\epsilon}_{ij}$ of the cylindrical sample is computed based on the best fit between the predicted and measured velocities for the set of particles contained within the sample using PFC [13]. The procedure actually relies on measuring the relative-to-average velocity of a particle, which is:

$$\tilde{V}_i^{(p)} = V_i^{(p)} - \bar{V}_i \tag{9}$$

where $V_i^{(p)}$ is a particle velocity and $\bar{V}_i$ is the average velocity of all particles in the discrete system. From a continuum mechanics point of view, the predicted relative velocity of a particle is related to the strain rate tensor and the location as follows:

$$\tilde{v}_i^{(p)} = \dot{\epsilon}_{ij}\tilde{x}_j^{(p)} \tag{10}$$

where $\tilde{x}_i^{(p)} = x_i^{(p)} - \bar{x}_i$ with $x_i^{(p)}$ denotes the position of a particle and $\bar{x}_i$ is the average position of all particles in the system. By taking the derivative of the sum of squared errors between predicted and measured velocities for all particles in the sample and setting it equal to zero, one can obtain the following system of equations [13]:

$$
\begin{bmatrix}
\sum_{N_p} \tilde{x}_1^{(p)} \tilde{x}_1^{(p)} & \sum_{N_p} \tilde{x}_2^{(p)} \tilde{x}_1^{(p)} & \sum_{N_p} \tilde{x}_3^{(p)} \tilde{x}_1^{(p)} \\
\sum_{N_p} \tilde{x}_1^{(p)} \tilde{x}_2^{(p)} & \sum_{N_p} \tilde{x}_2^{(p)} \tilde{x}_2^{(p)} & \sum_{N_p} \tilde{x}_3^{(p)} \tilde{x}_2^{(p)} \\
\sum_{N_p} \tilde{x}_1^{(p)} \tilde{x}_3^{(p)} & \sum_{N_p} \tilde{x}_2^{(p)} \tilde{x}_3^{(p)} & \sum_{N_p} \tilde{x}_3^{(p)} \tilde{x}_3^{(p)}
\end{bmatrix}
\begin{Bmatrix} \dot{\epsilon}_{i1} \\ \dot{\epsilon}_{i2} \\ \dot{\epsilon}_{i3} \end{Bmatrix}
=
\begin{Bmatrix} \sum_{N_p} \tilde{V}_i^{(p)} \tilde{x}_1^{(p)} \\ \sum_{N_p} \tilde{V}_i^{(p)} \tilde{x}_2^{(p)} \\ \sum_{N_p} \tilde{V}_i^{(p)} \tilde{x}_3^{(p)} \end{Bmatrix}
\tag{11}
$$

where i takes values of 1,2 and 3. The nine components of the matrix of the strain rate for the above system are obtained and by knowing the timestep of simulation, the homogenized strain matrix is obtained. Consequently, the volumetric strain is defined as the trace of the strain matrix: $\epsilon_v = \epsilon_{11} + \epsilon_{22} + \epsilon_{33}$. Furthermore, the Delaunay tessellation method offers an alternative approach for computing the strain matrix in granular assemblies [2] or from the deformation of membrane elements.

2.4 Evolution of pore pressure during undrained condition

In undrained triaxial tests, pore pressure evolves due to a constrained drainage while the material has a tendency to volume variations during shearing. As the soil undergoes shearing, pore water compression or expansion occurs, leading to an increase or decrease in pore water pressure. While coupling a DEM code with a computational fluid dynamics (CFD) code can simulate undrained condition for dynamic loading cases, employing CFD in quasi-static undrained tests may be impractical, as CFD primarily models fluid flow in dynamic conditions. In quasi-static undrained condition, fluid flow within the sample is negligible and pore pressure is considered as uniform throughout the sample. Consequently, the time evolution of pore pressure can be directly calculated from the changes in volumetric strain and the fluid Biot modulus M, given by $M = \frac{K_f}{n}$, where K_f and n are the effective fluid bulk modulus (if not perfectly saturated) and porosity, respectively. The effective confining stress σ'_c is updated as follows:

$$\frac{1}{M}\frac{\partial u}{\partial t} = \alpha_{Biot}\frac{\partial \epsilon_v}{\partial t} \tag{12}$$

$$\sigma'_c = \sigma_c - u \tag{13}$$

where σ_c is the applied confining stress. The term $\frac{\partial u}{\partial t}$ represents the variation of pore pressure with respect to time, where α_{Biot} denotes the Biot coefficient (assumed to be 1) and ϵ_v stands for the mechanical volumetric strain. The volumetric strain is determined at the end of each DEM cycle as discussed in Section 2.3. At the beginning of the next time step, Eq. 12 is employed to calculate the equivalent pore pressure, which is utilized in Eq. 13 to update the effective confining pressure only in the undrained condition. Where the confining pressure is applied on each node of triangular elements as an external force, as indicated in Eq. 1. The simulations remained stable despite incremental changes to the confining pressure, attributed to dynamic nature of Flac3D equation and the quasi-static simulations. If instability occurred, adjustments could be made incrementally to achieve equilibrium before applying updates.

3 Numerical packing and different models results for the drained condition

3.1 Numerical packing, generation procedures and model parameters.

For the purpose of investigating the effect of adopting either a membrane or another kind of boundary conditions in section 3.2, the generated DEM samples adopt different configurations. A rectangular parallelepiped with initial dimensions of L_Z=300mm,

L_X=200mm, L_Y=200mm is adopted both in the case of rigid walls and as the unit pattern for periodic boundaries, while a cylindrical sample with initial height h=300mm and a diameter D=200mm will include a flexible membrane boundary. DEM samples are prepared starting from a cloud of particles with no contacts. The number of particles is specified, and then the real PSD of the sand is scaled to fit this specified number of particles and the size of the specimen. As proven [20, Figure 6 therein] for the exact same sample preparation method used here, 7500 particles are sufficient to ensure a uniform distribution of porosity within a DEM sample. Furthermore, the stress-strain response remains unaffected when the number of particles exceeds this value. Therefore, in each simulation, the sample contains at least 7500 spheres, as shown in Table 1 and Fig. 2. The particle size distribution of Toyoura sand is used in these simulations as shown in Fig. 3, including a scaling factor. Simultaneously scaling the specimen dimensions and particle size for a same contact network is mechanically inconsequential in quasi-static cases due to the contact model, as the normal stiffness K_n value is normalized by particle size as shown in eq. A2. The sample is prepared by applying isotropic compaction, where the walls or membrane are moved towards the sample to achieve a target confining pressure. During the confining phase, the final porosity can be regulated by the friction coefficient and rolling coefficient independently of the subsequent shear loading phase, aiming to attain the same initial porosity values as those observed in the reference experimental data of Toyoura sand. In the case of the flexible membrane, the porosity is measured within a spherical measurement region positioned at the center of the cylindrical sample (since in the case of parallelepiped shape the porosity calculation is straightforward), with a diameter equal to 95% of the sample diameter. The contact parameters are provided in Table 1 based on the DEM model for Toyoura sand proposed by [18] after calibration and validation against experimental data. Finally, the quasi-static condition is guaranteed for the various triaxial tests by meeting the following specified condition for the inertia number: $I_r \leq 10^{-4}$ [6].

Since the membrane is firmly clamped around the top and bottom platens, the membrane can contribute to the strength of the material depending on its rigidity and its diameter. The rigidity parameters and membrane density are presented in Table 1, guided by the properties of the laboratory latex membrane [12]. The membrane is rather weak so that they can enclose the sample without contributing greatly to the material stiffness. Furthermore, the rolling friction between the shell elements and the adjacent particles as well as between the particles and the bottom and lower platen is eliminated.

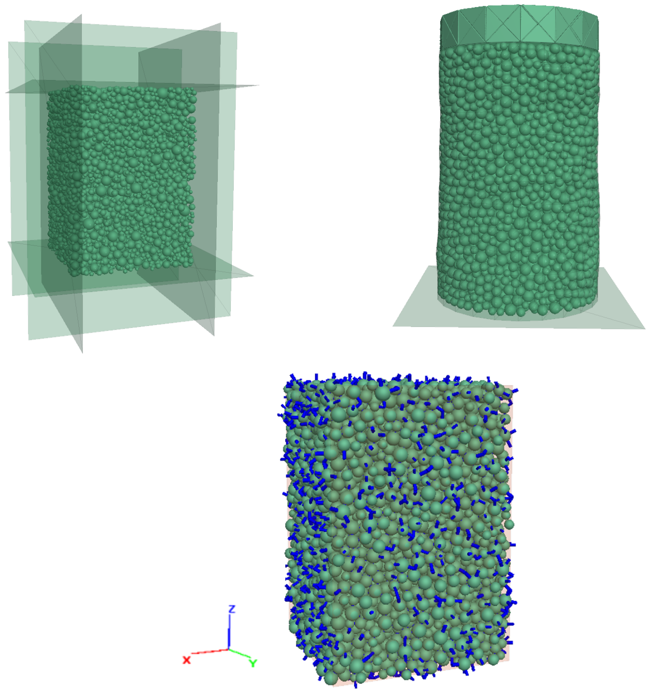

Fig. 2 Different 3D-DEM models with different boundary conditions: top-left rigid wall; top-right membrane; bottom periodic boundary.

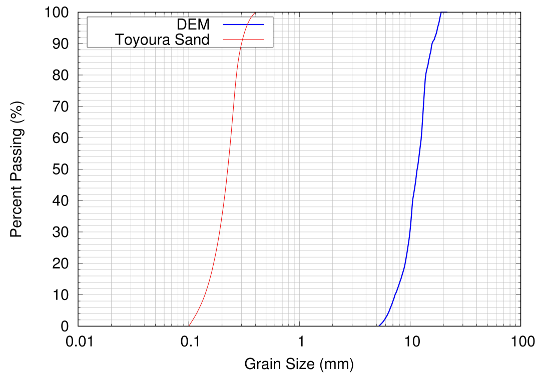

Fig. 3 Particle size distributions of Toyoura sand [after 8] vs DEM model employed for the different boundaries.

3.2 Effect of REV boundary conditions on the microscopic and macroscopic behavior

From the different types of boundary conditions described in Section 3.1, a comparison is made among the corresponding three different numerical models while keeping all other parameters constant, including the number of particles, initial void ratio, DEM contact model and strain rate. It is to note the common initial porosity adopted for all three DEM setups is in a remarkable agreement with the actual porosity of laboratory experiments proposed in [10] and used as a reference for the macroscopic behavior.

At a deeper scale, the microstructure is firstly assessed by examining both the evolution of the contact normal fabric tensor and the evolution of the coordination number during the triaxial test. The coordination number of an assembly of particles can be expressed as follows:

$$Z = \frac{2N_c}{N} \tag{14}$$

where N_c is the number of contacts and N is the number of bodies. The contact normal fabric tensor F_{ij} can be evaluated as follows:

$$F_{ij} = \frac{1}{N_c} \sum_{cont.} n_i \otimes n_j \tag{15}$$

where n_i is the contact normal direction. The anisotropy A of the fabric tensor F_{ij} is quantified and defined as the ratio between the second invariant of the fabric tensor and one third of the first invariant of the fabric tensor. Considering the axisymmetric condition of the triaxial test, the equation for anisotropy A leads to:

$$A = \frac{3(F_{11} - F_{33})}{F_{11} + 2F_{33}} = 3(F_{11} - F_{33}) \tag{16}$$

where the principal directions of the tensor F_{ij} are 1, 2 and 3, corresponding to the Z, X and Y directions respectively in the triaxial setting in Fig. 2. The fact that X, Y, Z are principal axes is no longer enforced beforehand by the numerical setup for the periodic and membrane boundary conditions (unlike the case of frictionless rigid walls). This property is checked in these cases and is still verified. Also, due to our preparation method of isotropic compaction on spherical particles, the principal directions of the fabric tensor are checked and found to be the same as the stress tensor.

The results at the microscopic level of the different simulations of 3D-DEM for the classical drained triaxial test with these different boundary conditions are shown in Fig. 4. The initial coordination number for the samples with different boundary conditions is close with a slight decrease for the rigid boundary condition. The initial anisotropy values for periodic boundaries and rigid wall is very close to zero. However, with a membrane boundary, there is an initial value for sample anisotropy. This is consistent with the results from experiments detailed in [31], which employed x-ray tomography on a laboratory triaxial cell containing nearly spherical particles. It indicates that a membrane boundary may induce initial fabric anisotropy, even when utilizing spherical particles within an isotropic stress state. During the shearing phase, the evolutions of the coordination number with the axial strain shows exactly the same trends. Furthermore, the evolution of the anisotropy of the sample with axial strain for the different models classically reveals the fact that the contacts tend to align with the direction of the applied load and therefore the anisotropy of the sample increases when increasing the axial strain. The different models exhibit a consistent tendency in the evolution of sample anisotropy, with a higher peak value observed for the periodic boundary condition. Additionally, specimens with a rigid boundary experience more pronounced fabric anisotropy during triaxial shearing compared to the sample with the membrane boundary under the same confining stress.

Secondly, a comparison on the macroscopic level is performed by which the stress-strain response of the three models will be presented. The macroscopic behavior of the model that uses the flexible membrane shows a high capability to fit the experimental data from [10] and especially the less dense sample as shown, in Fig. 5. Particularly, the membrane boundary provides a more accurate representation of the volumetric strain behavior. This advantage may be because of the flexible membrane has a higher degree of freedom than the rigid wall. This allows the sample to have a more dilatant volumetric behavior. Furthermore, the presence of friction between the platens and particles and the flexible membrane facilitates the presence of the shear band (loss of homogeneity, see Fig. 6) and mimics what is observed in the case of the laboratory triaxial test.

Table 1 DEM contact model, packing and membrane parameters

Contact				Packing		Membrane Properties			
$Emod$ (MPa)	k_n/k_s (-)	μ (-)	μ_r (-)	D_{min} - D_{max} (mm)	N (-)	E (MPa)	ν (-)	t (mm)	Density (kg/m^3)
450	3	0.6	0.38	4 - 20	7500 (min)	1	0.49	5	950

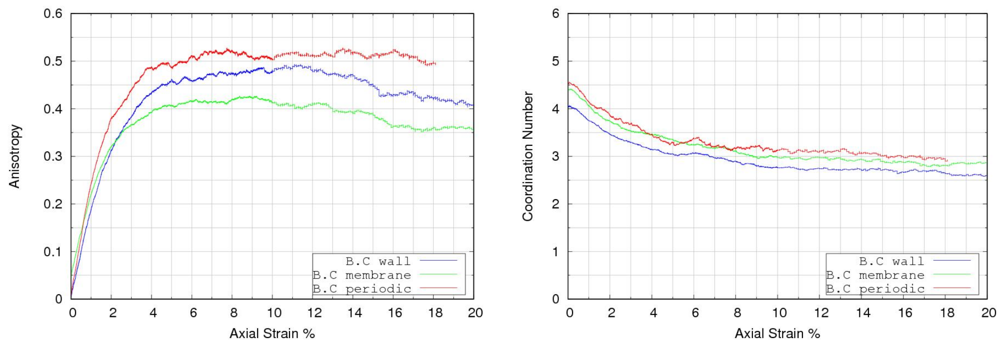

Fig. 4 Evolution of the fabric tensor and the coordination number during drained triaxial test for different boundary conditions with confining stress = 400 kPa and initial void ratio = 0.668.

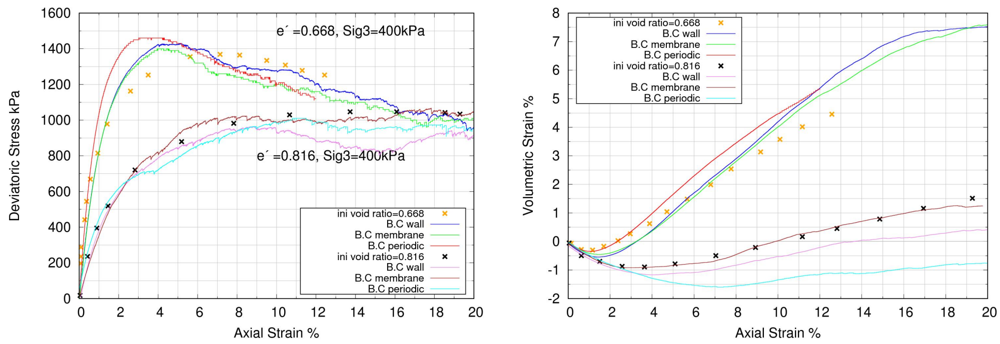

Fig. 5 Influence of the boundary condition on the macroscopic behavior. Cross points are experimental data [10] for a dense sample with an initial relative density D_r=91% and a relatively loose sample with an initial relative density D_r=50%.

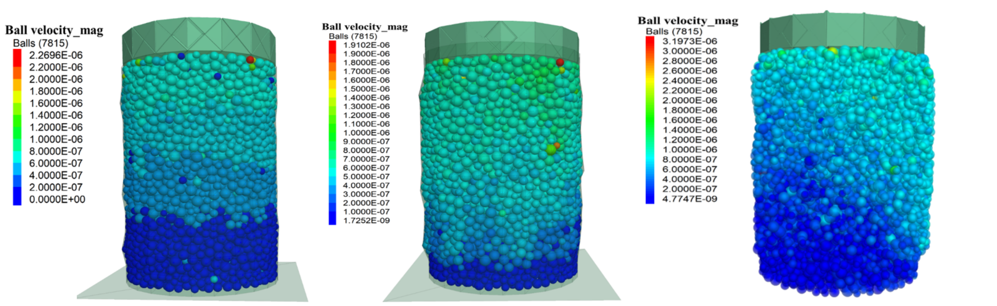

Fig. 6 Evolution of particles velocity field during the drained triaxial compression test with an initial void ratio of 0.668 (initial relative density D_r=91%) and a confining pressure of 400 kPa at different axial strain values: 0.05% (left), 3% (middle), 10% (right). Loss of strain homogeneity is evident at ϵ_{11}=10%

4 Undrained monotonic and cyclic triaxial tests

4.1 Undrained triaxial test with the membrane boundary condition

Fig. 7 presents the results of DEM simulations with the flexible membrane and different effective fluid bulk modulus K_f, alongside laboratory data from [33] for an undrained test with void ratio e = 0.79 and confining pressure 400 kPa. As expected, a higher K_f modulus results in a more pronounced increase in positive pore pressure, leading to a greater reduction in effective mean pressure, as illustrated in Fig. 8. In addition, the curve with $K_f = 8 \times 10^8 Pa$ aligns more closely with the experimental evolution of pore pressure, providing a better fit to the experimental data. The evolution of the strain matrix is shown in Fig. 8. The results show that in the case of the highest value of $K_f = 2 \times 10^9 Pa$, the variation of volumetric strain is nearly zero. However, a notable observation is that the loss of symmetry in horizontal strains ϵ_{xx} and ϵ_{yy}, along with the emergence of stress heterogeneity, becomes evident after the application of axial strain $\epsilon_a = 0.5\%$, as depicted in Figs 8 and 9. Fig. 9 shows that the difference between vertical stresses measured from the bottom and upper platen begins only after $\epsilon_a = 0.5\%$ and not from the beginning of the test. It is important to emphasize that the strain and stress heterogeneity induced by the membrane boundary cannot be accurately captured using a rigid wall boundary with the constant volume condition. In a constant volume setup, the lateral walls move uniformly to enforce a constant volume condition, resulting in the same strain in the horizontal directions. This uniform movement restricts the ability to simulate the realistic heterogeneity introduced by the flexible membrane boundary.

In reality, above the water table level, fluid saturation levels are typically less than 1, with high dissolved air content. The degree of saturation significantly influences the compressibility of the air–water mixture as indicated in [1]. One advantage of the proposed scheme is that it allows the estimation of pore pressure without imposing a constant volume condition. A direct relation can be established between Bulk modulus of water-gas mixture over water saturation. Also, the slightly unsaturated (quasi-saturated with only entrapped bubbles without capillary effect [17]) condition can be incorporated within this scheme. However, this would necessitate, in future work, the incorporation of more intricate equations for pore pressure evolution. [15] provides a means for directly managing and measuring pore pressure and water influx under unsaturated conditions. Alternatively, one can vary the effective fluid bulk modulus value of the sample to accommodate varying air content based on a specific law (e.g., making the K_f modulus proportional to pressure or volumetric change including capillary pressure [24]).

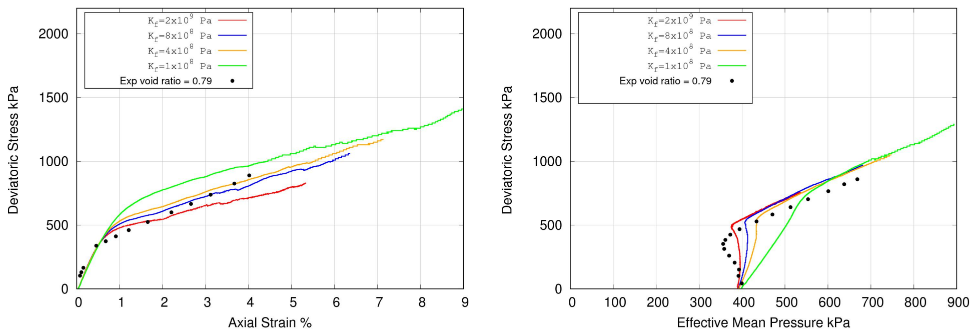

Fig. 7 Different undrained triaxial tests with different values of the effective fluid bulk modulus and with a confining pressure = 400 kPa and a void ratio = 0.79.

4.2 Undrained cyclic triaxial test with the membrane boundary condition

In undrained cyclic triaxial testing, as a sample undergoes liquefaction or significant deformation, the presence of a flexible membrane can contribute even more to the loss of homogeneity in the sample. In this context, a cyclic undrained triaxial test is conducted in Fig. 10 to explore the potential impact of a flexible membrane boundary

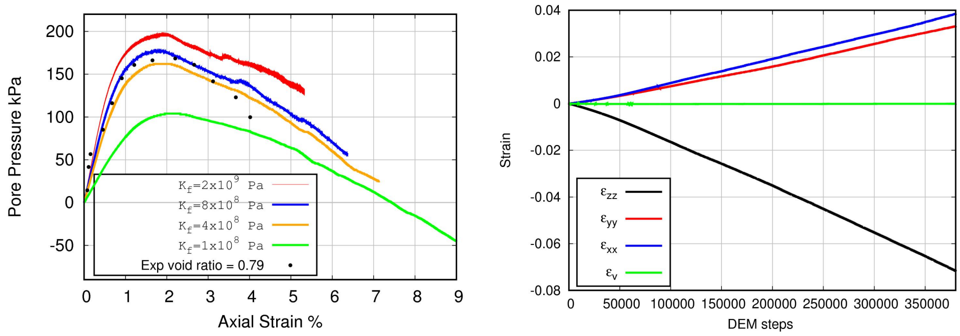

Fig. 8 Left: Evolution of pore pressure during an undrained triaxial test with different values of effective fluid bulk modulus K_f versus the experimental data. Right: Evolution of strain matrix and volumetric strain during an undrained triaxial test with $K_f = 2 \times 10^9 Pa$, a confining pressure = 400 kPa and a void ratio = 0.79.

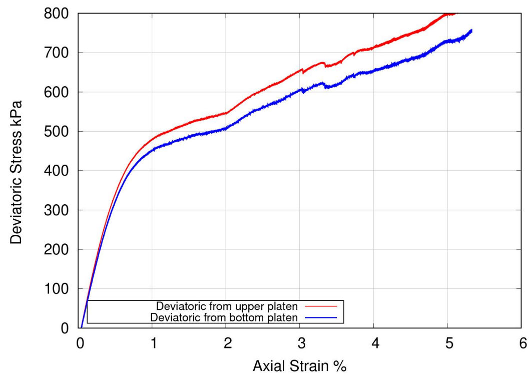

Fig. 9 Deviatoric stress measurements from upper and bottom platens during an undrained triaxial test with $K_f = 2 \times 10^9 Pa$, a confining pressure = 400 kPa and a void ratio = 0.79. The mismatch in external loads at these two boundaries may be attributed to stress heterogeneity along the sample rather than to a higher strain rate, as the difference began at $\epsilon_{zz} = 0.5\%$ and not from the beginning of the test.

on cyclic behavior. The test is performed at a confining pressure of $\sigma_3 = 400$ kPa and an initial void ratio of $e = 0.79$. The initial observation reveals that in comparison to different cyclic undrained triaxial tests conducted with the same DEM model (in terms of numerical parameters) for Toyoura sand but with a rigid wall boundary, presented in [20], the model with a flexible boundary exhibits greater axial deformation on the extension side than on the compression side, contradicting the DEM model with a rigid wall. This observation may be associated to the initially induced anisotropy value, indicating a preference for contact normals in the Z direction, in the case of the flexible boundary. This observation aligns with experimental data for undrained cyclic triaxial tests on Toyoura sand reported in various references such as [30, 34]. Additionally, there is a slight increase in the effective mean pressure at the beginning of the test see Figs. 10 and 11 even with fully saturated effective fluid bulk modulus (green curve in Fig. 11). This trend has consistently been observed in undrained cyclic tests conducted on Toyoura sand, as documented in the literature (e.g., [27, 30]). Additionally, these previous advantages compared to the experimental data are not observed when using a parallelepipedic cell with a periodic boundary condition [26]. Fig. 11 shows the effect of the value of effective fluid bulk modulus K_f on the mechanical behavior of the previous test. As expected, higher K_f value leads to more loss in effective mean pressure for the same number of cycles.

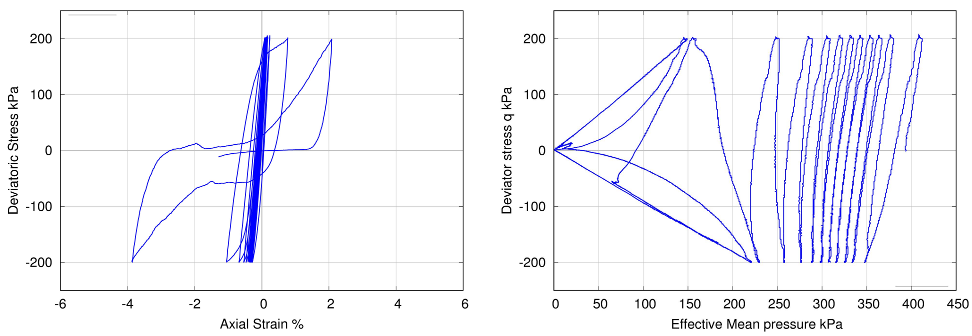

Fig. 10 Cyclic undrained triaxial tests using the membrane boundary with an effective fluid bulk modulus $K_f = 8 \times 10^8 Pa$, a confining pressure = 400 kPa and a void ratio = 0.79.

5 Conclusion

This paper presents DEM simulations of drained and undrained conditions of triaxial tests using a membrane boundary condition. The membrane boundary is simulated by utilizing the constant strain triangle (CST) via FEM with central-difference method for time integration, inducing membrane action in shell elements. The shell element is characterized by four parameters: Young's modulus E, Poisson's ratio ν, membrane

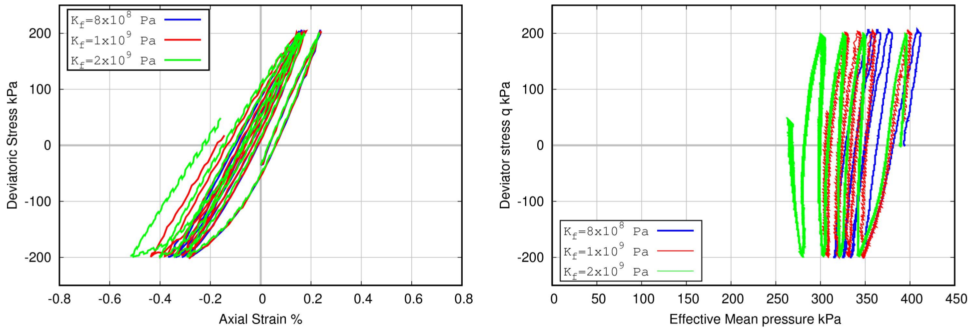

Fig. 11 Effect of different K_f values on the cyclic undrained behavior with the flexible boundary condition.

thickness t and density ρ. An equivalent force system for contact forces and induced by the interaction with the granular sample is applied to the nodes of triangular elements. Also, the full strain matrix is estimated to compute the volumetric strain and assess strain heterogeneity in samples with the flexible boundary. Furthermore, the excess pore pressure during the undrained condition is computed based on the variation of the volumetric strain and the effective fluid bulk modulus K_f. The corresponding effective confining pressure is updated to include the evolution of the excess pore pressure.

A DEM model containing approximately 7500 spherical particles is used, along with a rolling resistance contact model that has already been calibrated and validated for Toyoura sand. In drained triaxial condition, a comparison is made between flexible membrane, rigid wall and periodic boundaries. At the microscopic level and for the same void ratio, the membrane boundary exhibits an initial value for fabric anisotropy after the isotropic compaction phase, while both periodic and rigid wall boundaries show a zero initial fabric anisotropy. At the macroscopic level, the evolution of deviatoric stress is identical for rigid and membrane boundaries until reaching the peak. However, differences become more pronounced during the post-peak stage. Regarding the evolution of the volumetric strain, the membrane boundary demonstrates a higher capability than the other boundaries in fitting experimental data for loose and mid-dense samples of Toyoura sand. Also, shear band evolution during drained test with the flexible boundary for mid dense sample was observed. Also, the flexible boundary is used to simulate undrained triaxial tests for Toyoura sand. Using the highest value of the effective bulk modulus $K_f = 2 \times 10^9 Pa$ indicating a saturated condition shows nearly zero evolution in the volumetric strain. Furthermore, the results of this test exhibit good agreement with the experimental data of Toyoura sand in both the deviatoric and effective stress curves. Additionally, an examination of stress heterogeneity and different lateral strains induced by flexible membrane is highlighted by measuring deviatoric stress from the upper and bottom platens of the triaxial cell, as well as from the strain matrix. Differences between lateral strains ϵ_{xx} and ϵ_{yy}, as well as between the deviatoric stress measured from the bottom and upper platen, are observed after axial strain $\epsilon_a = 1\%$, implying heterogeneity in stress within the sample. Finally, a cyclic undrained test is conducted, revealing two main observations. First, by using a rigid wall boundary and the same numerical parameters, it was observed that there is more axial strain on the compression side for the same number of cycles, contradicting the experimental data. However, the results with a flexible membrane show more axial strain on the extension side. Second, at the beginning of the test, a slight increase in effective mean pressure is observed similar to many experimental tests for cyclic and monotonic undrained tests in the literature.

The perspective of this work involves studying the mechanical behavior and shear band formation of the DEM model with irregular polyhedron particles for Toyoura sand presented in [18], incorporating the flexible boundary condition proposed in this study. Another aspect is the examination of quasi-saturated behavior under triaxial undrained condition using the DEM model with the flexible boundary condition.

Acknowledgements

The authors would like to express their thanks to the Itasca Educational Partnership Program (IEP, Zhao Cheng and Sacha Emam) for its valuable support and for providing PFC software. The First author would like to particularly thank Dr. Denis Martinand (Aix-Marseille University, France) for discussing and providing valuable feedback.

Appendix A Contact model

An elastic normal contact force evolves in the following manner:

$$\vec{f_n} = K_n \vec{\delta}_n \tag{A1}$$

$$K_n = E_{mod} \frac{\pi r^2}{R_1 + R_2} \ with \ r = \begin{cases} R_1 + R_2, \text{ particle-particle} \\ R_1, \text{ particle-shell element.} \end{cases} \tag{A2}$$

where $\vec{\delta}_n$ is the relative normal-displacement and K_n, E_{mod} are the normal stiffness and normalized parameter. R_1 and R_2 are the radii of the two contacting spheres. In the case of contact between a particle and a shell element, the radius R_2 represents the radius of the shell element and is equal to zero. The shear force is :

$$\vec{f_s} = \vec{f_s^0} + K_s \Delta \vec{\delta}_s \tag{A3}$$

where $\vec{f_s^0}$ and $\vec{\delta}_s$ are the shear force and the shear displacement at the beginning of a time step. K_s is the contact tangential stiffness. The Coulomb friction condition is imposed as follows:

$$||\vec{f_s}|| \leq ||\vec{f_n}||\mu \tag{A4}$$

where μ is the coefficient of friction. The rolling stiffness and moment incremental laws are as follows:

$$K_r = K_s R_m^2 \tag{A5}$$

$$\frac{1}{R_m} = \frac{1}{R_1} + \frac{1}{R_2} \tag{A6}$$

$$\Delta\vec{M}_r = K_r \Delta\vec{\theta}_b \quad ||\vec{M}_r|| \leq \mu_r ||\vec{f}_n|| R_m \tag{A7}$$

$$\Delta\vec{\theta}_b = \Delta\vec{\theta} - \Delta\theta_t.\vec{n}_c \tag{A8}$$

where $\vec{n}_c$ is contact normal, μ_r, R_m, $\Delta\vec{\theta}$, $\Delta\theta_t$ and $\Delta\vec{\theta}_b$ represent the rolling friction coefficient, effective radius, rotation increment, relative twist-rotation increment and relative bend-rotation increment, respectively.

Declaration of competing interest

The authors declare the following financial interests/personal relationships which may be considered as potential competing interests: The commercial softwares used for this study have been provided within the Itasca Educational Partnership (IEP) Research Program which is gratefully acknowledged.

Data availability

Some or all data, models, or codes that support the findings of this study are available from the corresponding author upon reasonable request.

References

[1] Chaney R (1978) Saturation effects on the cyclic strength of sands. In: Earthquake Engineering and Soil Dynamics–Proceedings of the ASCE Geotechnical Engineering Division Specialty Conference. volume I. ASCE, New York, pp 432–357

[2] Chueire J, Daouadji A, Nicot F, et al (2023) On the extension of the grain loop concept from 2d to 3d granular assemblies. Granular Matter 25(3):57

[3] Cil MB, Alshibli KA (2014) 3d analysis of kinematic behavior of granular materials in triaxial testing using dem with flexible membrane boundary. Acta Geotechnica 9:287–298

[4] Cook RD, et al (1989) Concepts and applications of finite element analysis. John wiley & sons

[5] Cundall P (1988) Computer simulations of dense sphere assemblies. In: Studies in Applied Mechanics, vol 20. Elsevier, p 113–123

[6] Da Cruz F, Emam S, Prochnow M, et al (2005) Rheophysics of dense granular materials: Discrete simulation of plane shear flows. Physical Review E 72(2):021309

[7] De Bono J, McDowell G, Wanatowski D (2012) Discrete element modelling of a flexible membrane for triaxial testing of granular material at high pressures. Géotechnique Letters 2(4):199–203

[8] Dong Q, Xu C, Cai Y, et al (2016) Drained instability in loose granular material. International Journal of Geomechanics 16(2):04015043

[9] Duriez J, Wan R, Pouragha M, et al (2018) Revisiting the existence of an effective stress for wet granular soils with micromechanics. International Journal for Numerical and Analytical Methods in Geomechanics 42(8):959–978. https://doi.org/10.1002/nag.2774

[10] Fukushima S, Tatsuoka F (1984) Strength and deformation characteristics of saturated sand at extremely low pressures. Soils and Foundations 24(4):30–48

[11] Götz H, Pöschel T (2023) Dem-simulation of thin elastic membranes interacting with a granulate. Granular Matter 25(4):61

[12] Henkel D, Gilbert G (1952) The effect measured of the rubber membrane on the triaxial compression strength of clay samples. Geotechnique 3(1):20–29

[13] Itasca (2018) Pfc — particle flow code, ver. 6.0. Itasca Consulting Group, Inc.

[14] Itasca (2019) Flac3d - fast lagrangian analysis of continua in three dimensions, version 7.0. Itasca Consulting Group, Inc.

[15] Kuhn MR, Daouadji A (2020) Simulation of undrained quasi-saturated soil with pore pressure measurements using a discrete element (dem) algorithm. Soils and Foundations 60(5):1097–1111

[16] Li Z, Chow JK, Li J, et al (2022) Modeling of flexible membrane boundary using discrete element method for drained/undrained triaxial test. Computers and Geotechnics 145:104687

[17] Miot M, Veylon G, Wautier A, et al (2021) Numerical analysis of capillary bridges and coalescence in a triplet of spheres. Granular Matter 23(3):65

[18] Mohamed T, Duriez J, Veylon G, et al (2022) DEM models using direct and indirect shape descriptions for toyoura sand along monotonous loading paths. Computers and Geotechnics 142:104551. https://doi.org/10.1016/j.compgeo.2021.104551

[19] Mohamed T, Duriez J, Veylon G, et al (2023) A 3d-dem model for tropical residual soils under monotonic and cyclic loadings. Journal of Geotechnical and Geoenvironmental Engineering 149(11):04023094. https://doi.org/10.1061/JGGEFK.GTENG-11323

[20] Mohamed T, Duriez J, Veylon G, et al (2023) A discrete-based multi-scale modeling approach for the propagation of seismic waves in soils. Soil Dynamics and

Earthquake Engineering 173:108104. https://doi.org/https://doi.org/10.1016/j.soildyn.2023.108104, URL https://www.sciencedirect.com/science/article/pii/S0267726123003494

[21] Qu T, Feng Y, Wang Y, et al (2019) Discrete element modelling of flexible membrane boundaries for triaxial tests. Computers and Geotechnics 115:103154

[22] Qu Y, Zou D, Liu J, et al (2022) Two-dimensional dem-fem coupling analysis of seismic failure and anti-seismic measures for concrete faced rockfill dam. Computers and Geotechnics 151:104950

[23] Radjai F, Voivret C (2011) Periodic boundary conditions. In: Radjai F, Dubois F (eds) Discrete-element Modeling of Granular Materials. ISTE-Wiley

[24] Rozhko AY (2020) Effective fluid bulk modulus in the partially saturated rock and the amplitude dispersion effects. Journal of Geophysical Research: Solid Earth 125(3):e2019JB018693

[25] Sibille L, Hadda N, Nicot F, et al (2015) Granular plasticity, a contribution from discrete mechanics. Journal of the Mechanics and Physics of Solids 75:119–139

[26] Sibille L, Benahmed N, Darve F (2021) Constitutive response predictions of both dense and loose soils with a discrete element model. Computers and Geotechnics 135:104161

[27] Toyota H, Takada S (2022) Mechanical properties of cementitious sand and sand with small cyclic shear strain to assess aging effects on liquefaction. Acta Geotechnica 17(7):2825–2840

[28] Vermeer P (1990) The orientation of shear bands in biaxial tests. Géotechnique 40(2):223–236

[29] Villard P, Chevalier B, Le Hello B, et al (2009) Coupling between finite and discrete element methods for the modelling of earth structures reinforced by geosynthetic. Computers and Geotechnics 36(5):709–717

[30] Wang R, Fu P, Zhang JM, et al (2016) Dem study of fabric features governing undrained post-liquefaction shear deformation of sand. Acta Geotechnica 11(6):1321–1337

[31] Wiebicke M, Andò E, Viggiani G, et al (2020) Measuring the evolution of contact fabric in shear bands with x-ray tomography. Acta Geotechnica 15(1):79–93

[32] Wu K, Sun W, Liu S, et al (2021) Study of shear behavior of granular materials by 3d dem simulation of the triaxial test in the membrane boundary condition. Advanced Powder Technology 32(4):1145–1156

[33] Yoshimine M (2013) Yoshimine m. archives – soil mechanics laboratory. Tokyo Metro-politan

[34] Zhao J, Guo N (2013) Unique critical state characteristics in granular media considering fabric anisotropy. Géotechnique 63(8):695–704